



OPEN

Anisotropic Superconducting Gap and Elongated Vortices with Caroli-De Gennes-Matricon States in the New Superconductor $Ta_4Pd_3Te_{16}$

SUBJECT AREAS:

SUPERCONDUCTING
PROPERTIES AND
MATERIALS

CONDENSED-MATTER PHYSICS

Received

8 January 2015

Accepted

2 March 2015

Published

23 March 2015

Correspondence and requests for materials should be addressed to H.Y. (huanyang@nju.edu.cn) or H.-H.W. (hhwen@nju.edu.cn)

Zengyi Du, Delong Fang, Zhenyu Wang, Yufeng Li, Guan Du, Huan Yang, Xiyu Zhu & Hai-Hu Wen

Center for Superconducting Physics and Materials, National Laboratory of Solid State Microstructures and Department of Physics, Collaborative Innovation Center for Advanced Microstructures, Nanjing University, Nanjing 210093, China.

The superconducting state is formed by the condensation of a large number of Cooper pairs. The normal state electronic properties can give significant influence on the superconducting state. For usual type-II superconductors, the vortices are cylinder like with a round cross-section. For many two dimensional superconductors, such as Cuprates, albeit the in-plane anisotropy, the vortices generally have a round shape. In this paper we report results based on the scanning tunnelling microscopy/spectroscopy measurements on a newly discovered superconductor $Ta_4Pd_3Te_{16}$. The chain-like conducting channels of $PdTe_2$ in $Ta_4Pd_3Te_{16}$ make a significant anisotropy of the in-plane Fermi velocity. We suggest at least one anisotropic superconducting gap with gap minima or possible node exists in this multiband system. In addition, elongated vortices are observed with an anisotropy of $\xi_{||b}/\xi_{\perp b} \approx 2.5$. Clear Caroli-de Gennes-Matricon states are also observed within the vortex cores. Our results will initiate the study on the elongated vortices and superconducting mechanism in the new superconductor $Ta_4Pd_3Te_{16}$.

For a type-II superconductor, magnetic flux will penetrate into the bulk and form the quantized vortices when the external magnetic field exceeds the lower critical value H_{c1} . For most conventional superconductors, the vortices are cylinder-like with a round cross-section. For cuprate superconductors, pancake vortices with the round or four-fold symmetric shape have been observed¹⁻⁴. In 2H-NbSe₂ superconductor a 6-fold symmetrical shape of vortices has been discovered^{5,6}. In iron based superconductors, the vortices seem to have a round or four-fold symmetric shape in many systems⁷⁻⁹. It is quite rare to observe a twofold symmetric shape (elongated) of vortices. Elongated vortices are expected in the Josephson vortex systems when the magnetic field is parallel to the ab -planes in 2D superconductors¹⁰⁻¹³. Occasionally, single elongated vortex may be observed on the basal plane when the supercurrent is confined by the C_2 like electronic state on FeSe film¹⁴ or in the state with electronic nematicity. Recently superconductivity with the $PdTe_2$ chains as the conducting channels¹⁵ was discovered in $Ta_4Pd_3Te_{16}$ (Ref. 16). Band structure DFT calculations reveal a mixture of 1D, 2D and 3D Fermi surfaces in this system¹⁷. Recent thermal conductivity measurements¹⁸ show the sizable residual thermal conductivity coefficient $\kappa/T|_{T \rightarrow 0}$ and its $H^{1/2}$ magnetic field dependence under magnetic field, suggesting a nodal gap structure. It is thus curious to know how the superconducting gaps look like. Concerning the one dimensional conduction in the $PdTe_2$ -chain based superconductors, it is also desired to see whether the vortices are present, and in what form? If the Fermi surface structure contains an 1D component, the anisotropic in-plane Fermi velocity may lead to the elongation of vortex core structure. For these elongated vortices, how about the Abrikosov lattice? Furthermore, it would be very interesting to know how the Caroli-de Gennes-Matricon (CdGM) states^{19,20} distribute spatially within the vortex cores with a strong one dimensional component.

Results

Sample characterization and surface topography. The $Ta_4Pd_3Te_{16}$ single crystal samples were grown using self-flux method. The needle-like single crystals have the typical dimensions of about $2 \times 0.2 \times 0.1$ mm³. The superconducting transition occurs at about 4.5 K and is characterized by resistivity and DC magnetic susceptibility measurements, as shown in Figs. 1(c) and (d) respectively. The long-rod shape of the samples with shiny top-surfaces provides information on the anisotropic crystal structures. This material is a layered system with the

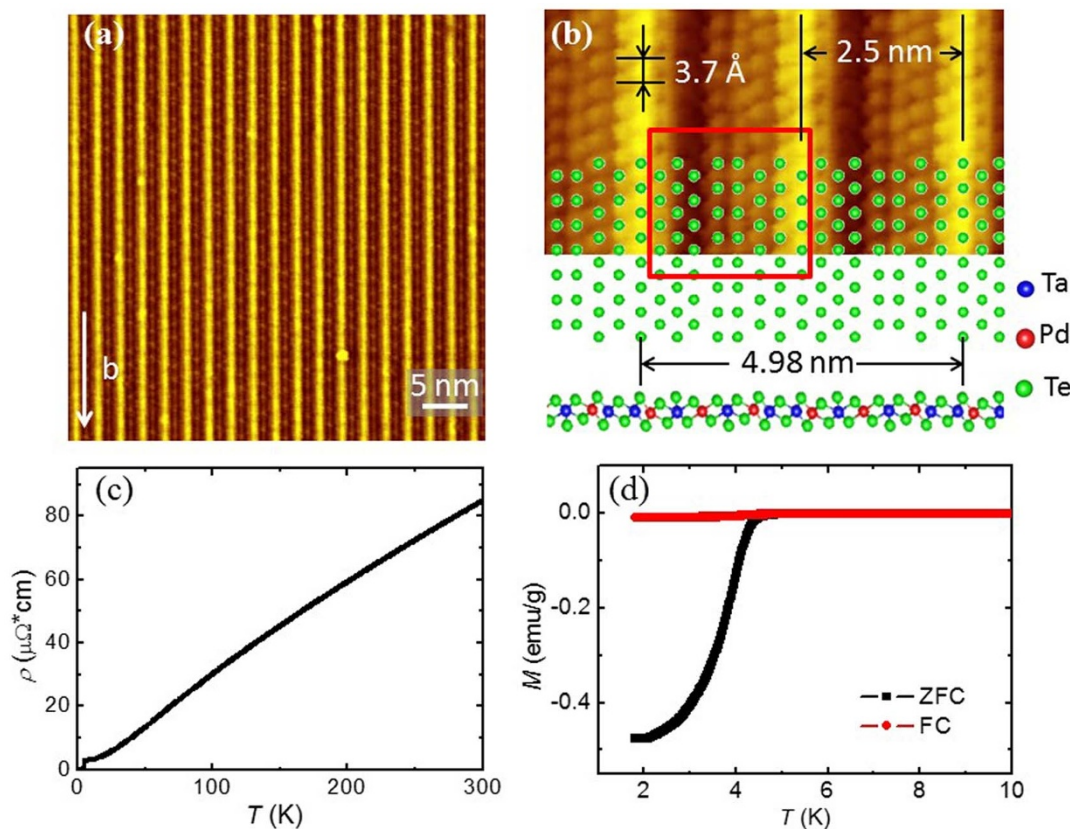


Figure 1 | STM topographies and superconducting transitions of $\text{Ta}_4\text{Pd}_3\text{Te}_{16}$. (a), An atomically resolved topography at bias voltage $V_{\text{bias}} = 100$ mV and tunnelling current $I_t = 50$ pA. (b), A zoom-in view of the image in (a) and the corresponding crystal structure projected along the $[-1\ 0\ 3]$ (upper) and $[010]$ (lower) directions. $V_{\text{bias}} = 30$ mV, $I_t = 100$ pA. (c,d), Temperature dependence of resistivity and magnetization after zero-field cooling and field cooling at 10 Oe.

stoichiometric composition for each individual layer along (-103) direction, so it is very easy to cleave and the charge-neutral plane with Te atoms on the top surface will be obtained. Figure 1(a) represents a topographic image of a cleaved surface in an area of 50×50 nm². According to the crystal structure, the surface termination has no other choices but Te atoms. A stripe like feature is observed, with a spatial distance between the unidirectional bright chains of about 2.5 nm. Because the Ta atoms have the largest radii among the three kinds of elements in the compound, and the Te atoms on the top layer sitting just above two neighbour linear Ta atom chains have higher heights, this may explain the appearance of the bright chains. Through a closer scrutiny on the atomic structure as shown in the upper panel of Fig. 1(b), we find that the period distance of the neighbored chains on top-surface is exactly equal to the distance of the PdTe_2 chains of $\text{Ta}_4\text{Pd}_3\text{Te}_{16}$. Along each chain, one can find that the atoms arrange themselves in an alternative way with the distance between two neighbour atoms of about 3.7 Å which is consistent with the lattice constant b of the material. Thus the b -axis of the crystal must be along the bright chains. It is interesting to note that between the neighboring bright chains, some kind of periodic bright spots with a larger scale than the atomic lattice parameter along b -axis was observed in Fig. 1(a). These bright spots assembled in a rhombus lattice form may be induced by the surface reconstruction or the charge density wave modulations, which needs further investigation. When we try to match the atomic pattern with the surface Te atoms as shown in the bottom panel of Fig. 1(b), we find that the measured atoms in some 2.5 nm period regions marked with red rectangle have a shift with a half lattice parameter b from the expectation of the structure, i.e., the exact lattice periodicity is 5 nm while the real one measured is 2.5 nm. In short summary, the atomic structure is con-

sistent with the model configuration of the $\text{Ta}_4\text{Pd}_3\text{Te}_{16}$ phase, beside the lattice shift a half lattice constant along b -axis.

Scanning Tunneling Spectroscopy (STS). STS is a direct probe to detect the local density of states (DOS), which can provide key information on the superconducting gap symmetry. In Fig. 2(b), we show the STS data measured at 0.45 K by having a line scan of the spectra along the blue arrowed line crossing several bright chains on the surface shown in Fig. 2(a). Although here the top surface is not atomically resolved, the distance between two neighboring bright chains is the same as that in Fig. 1(a). The superconducting feature is very clear here, and the low-energy part of the spectrum seems to be very homogenous and is perfectly reproducible. The spectra present two symmetric superconducting coherence peaks at energies of about ± 0.95 mV. In the superconducting state, the differential conductance at the Fermi energy shows at least a 90% decrease from the normal state, which may provide some hints on gap symmetry. The shape of the spectra near the Fermi energy is close to the V-shape with a smeared bottom and is reminiscent of that in Cuprates²¹ or Chevrel phase family of superconductor PdMo_6S_8 (Ref. 22). Before this work, the measurements of thermal conductivity in $\text{Ta}_4\text{Pd}_3\text{Te}_{16}$ suggest that there may exist nodes in the gap functions¹⁸. However, theoretical calculation shows that $\text{Ta}_4\text{Pd}_3\text{Te}_{16}$ may be a conventional s -wave superconductor¹⁷ with Cooper pairs arising from the p -orbital electrons.

Discussion

In order to classify this point, we present a typical normalized STS spectrum measured at 0.45 K divided by the one taken at 5 K and show in Figs. 2(c) and (d) as symbols. Meanwhile we fit the data with

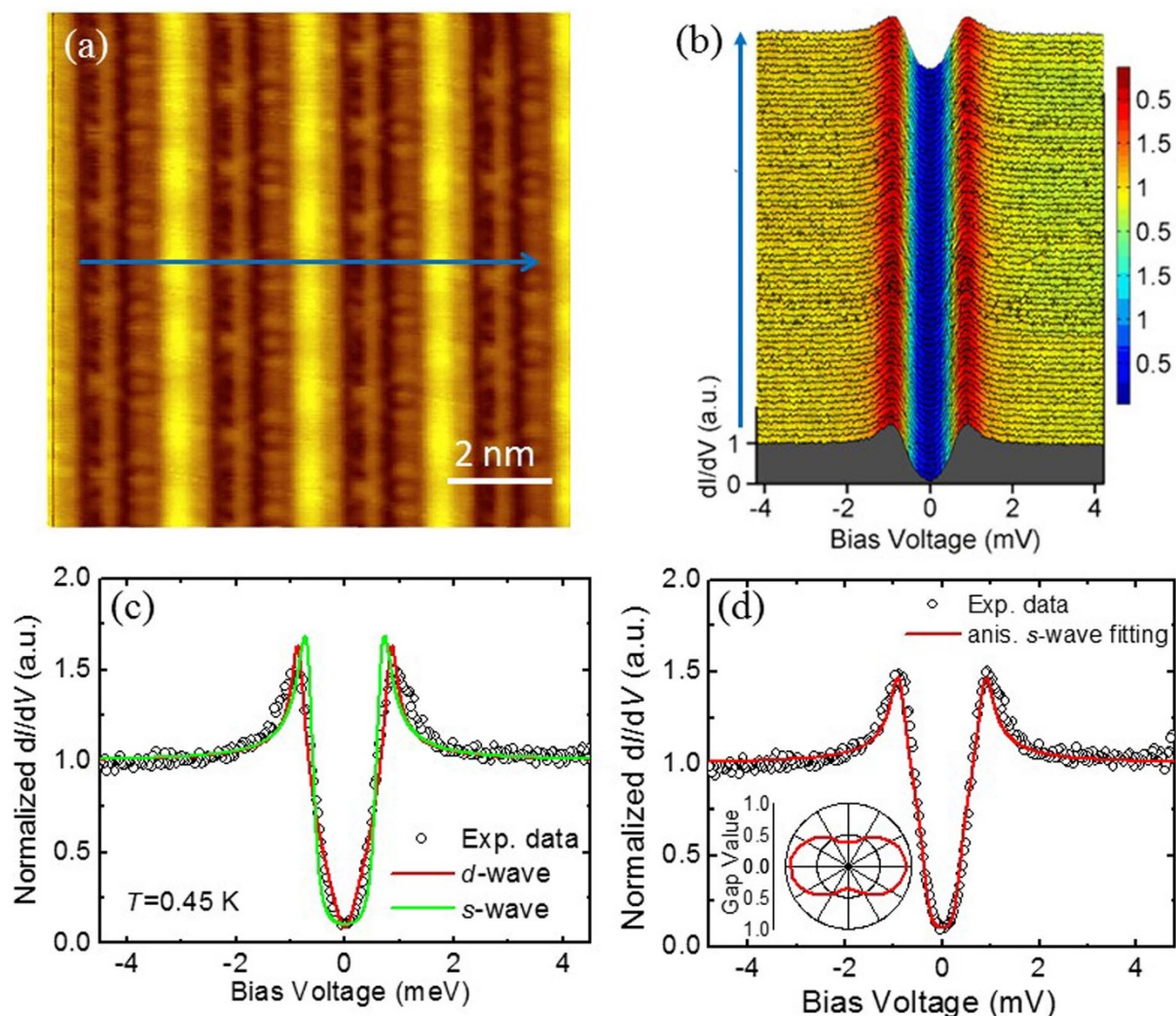


Figure 2 | STS spectra and theoretical fitting with different gap functions. (a), Topographic image ($V_{\text{bias}} = 100$ mV, $I_t = 50$ pA). The blue arrow indicates the trace on which the tunnelling spectra shown in (b) were measured. (b), The spatially resolved tunnelling spectra dI/dV versus V at 0.45 K. (c,d), Fitting results to a typical STS spectrum at 0.45 K normalized by the one measured in the normal state (at 5 K). The symbols represent the experimental data, and the coloured lines are the theoretical fits to the data with the Dynes model with d -wave, s -wave and an anisotropic s -wave gap, respectively. The inset in (b) shows a twofold symmetric gap function $\Delta = 0.644 + 0.276\cos 2\theta$ (meV) yielded from the fitting with an anisotropic s -wave gap.

several scenarios of superconducting gaps based on the Dynes model²³, these include a single isotropic s -wave gap, a single d -wave gap, an anisotropic s -wave gap, as shown in Figs. 2(c) and (d). Since there are multibands in the compound $\text{Ta}_4\text{Pd}_3\text{Te}_{16}$ (Ref. 17), we also used two components ($s_1 + s_2$ or $s + d$) of differential conductivity with each containing a single gap function (either s - or d -wave), instead of using one component but with a mixture of two gaps (see Supplementary Information SI-I). We must emphasize that all the fittings in this Report are the optimized ones yielding the reliable parameters. The results based on s -wave and d -wave fitting are plotted together with the experimental data in Fig. 2(c). For the s -wave fitting, as shown by the green solid line, the calculation fails to track the low energy line shape, which always displays a more flat bottom of local DOS near the Fermi energy compared with the experimental data. On the other hand, the fitting with a single d -wave gap, although has a better global fit to the STS curve, but generates a “V-shape” feature near the bottom, which also deviates from the experimental data. Because the single isotropic s -wave and d -wave pairing symmetry cannot appropriately interpret our data, we use an anisotropic s -wave gap function to simulate the data. Although a twofold or a four-fold symmetric gap functions would lead to the

STS with the same shape, since the material has the PdTe_2 chains as the conducting channels, we use a twofold-symmetric anisotropic s -wave function $\Delta(\theta) = \Delta_1 + \Delta_2 \cos 2\theta$ instead of a four-fold symmetric gap function. The best fit to the spectrum leads to $\Delta_1 = 0.644$ meV and $\Delta_2 = 0.276$ meV. For details of the fitting one is referred to the SI-I. As shown in Fig. 2(d), the anisotropic s -wave model can fit the data quite nicely, both near the bottom and the coherence peaks. The gap function is shown in the inset of Fig. 2(d) in a blue dumbbell like shape with a minimum value 0.37 meV and maximum value 0.92 meV. Taking the maximum gap value we determined $2\Delta_{\text{max}}/k_B T_c \approx 4.6$. We also fit the spectra with $s + d$ waves and present in Fig. S1(b), the fitting is as good as the one with anisotropic s -wave (SI-I). So we argue that the superconducting gap is highly anisotropic, or even there exist nodes or gap zero on the superconducting gap(s). Further experiments are required to resolve the issue whether the superconducting gap has a node or not.

Magnetic vortices appear in the mixed state for a type-II superconductor when a magnetic field is applied. The vortex core size can roughly give the coherence length ξ . Next we focus on the measurements under an applied magnetic field. Since the upper critical field H_{c2} perpendicular to the cleavage surface is about 3 T, in order to



maintain a less-suppressed superfluid density outside the vortex core, we applied a magnetic field of 0.8 T with orientation perpendicular to the cleavage surface. Figure 3(a) shows a 2D mapping of the zero bias conductance (ZBC) over an area of $180 \times 180 \text{ nm}^2$. In order to visualize the vortex more clearly, we filled out the signal associating with the bright chains (see SI-II). Strikingly, one can see that the vortex is elongated along the b -axis, i.e., the typical size is around 45 nm in the b -axis and 22 nm vertical to the b -axis, which may reveal the anisotropy of electronic properties in the cleavage plane. The average flux per vortex calculated from our data is about $1.99 \times 10^{-15} \text{ Wb}$, being close to the single magnetic flux quanta $2.07 \times 10^{-15} \text{ Wb}$. It is known that the coherence length is proportional to Fermi velocity and inversely proportional to the gap amplitude, expressed as $\xi = \hbar v_F / \pi \Delta$. According to the theoretical calculation of the Fermi surface¹⁷ and the gap anisotropy in this Report, the elongation can be understood qualitatively. In addition, we find that the Abrikosov lattice is also distorted along the b -axis, but still with a basic triangle lattice. A close scrutiny can find that the three angles enclosed by the three neighbor vortices are: 45° , 74° , and 61° , as highlighted by red triangle in Fig. 3(a). At a position with more symmetric vortex structure, we find the three angles of about: 48° , 66° , and 66° . An elongation of the vortex lattice along b -axis is evidently observed. The distorted vortex lattice with the elongated vortices observed here may be described by the model concerning in-plane anisotropic penetration depth or the coherence length. Theoretically an elongated structure of vortex and a distorted vortex lattice were predicted²⁴ for uniaxial superconductors (anisotropy between c -axis and ab -planes) when the magnetic field is applied deviating from c -axis. Detailed and quantitative analysis on the vortex structure and the distorted vortex lattice in present work is underway.

Figure 3(b) displays a series of the spectra taken along the arrowed line crossing vortex centre as shown in Fig. 3(c) at a magnetic field of 0.8 T. The apparent CdGM bound state peak is clearly observed

around the vortex core centre. Away from the vortex core center, the bound state disappears and the spectrum evolves continuously towards outside the vortex. When we divide the STS measured at the vortex core centre by that away from vortex centre, the CdGM state (Fig. 3(d)) becomes more obvious and a peak locates around the Fermi energy. On the other hand, the density of states at the Fermi energy decreases about 20% and the superconducting coherence peaks are suppressed dramatically outside the vortex core, indicating that the supercurrent outside the vortex core may smear up the gapped feature through the Doppler shift^{25,26} if the gap has a nodal or highly anisotropic structure in $\text{Ta}_4\text{Pd}_3\text{Te}_{16}$. We will further address this issue in the following.

In order to evaluate how strong the anisotropy of the vortex is and the superfluid distribution around a vortex, we measured the spectra far away from the vortex core (near the symmetric position of the four neighbor vortices) as shown in Fig. 4(b) with an external field of 0.8 T, and with the magnetic field released to zero as shown in Fig. 4(a). The two set of data were measured by going through exactly the same trace with a scanning distance of about 7.5 nm. It is clear that the DOS at zero bias dropped more than 80% when the field is zero, but it drops only about 15% when magnetic field is applied. The difference between the STS outside the vortex core in Fig. 3(b) and 4(b) may be induced by the different positions or the surface inhomogeneity. This weak suppression to the DOS at zero energy outside a vortex core is counterintuitive for an s -wave superconductor, since the superconducting order parameter will be established quickly outside the vortex core with a distance of about ξ . However, for a superconductor with strong gap anisotropy or nodes, the Doppler shift^{25,26} will induce a finite DOS at E_F in the region $\lambda_L > r > \xi$ (r the radial distance from the core center, λ_L is the London penetration depth). The strong suppression of the superconducting coherence peak and significant lifting of the ZBC far away from the vortex core centre certainly suggests a gap minimum or zero gap on the gap function. To extract the superconducting coherence length ξ ,

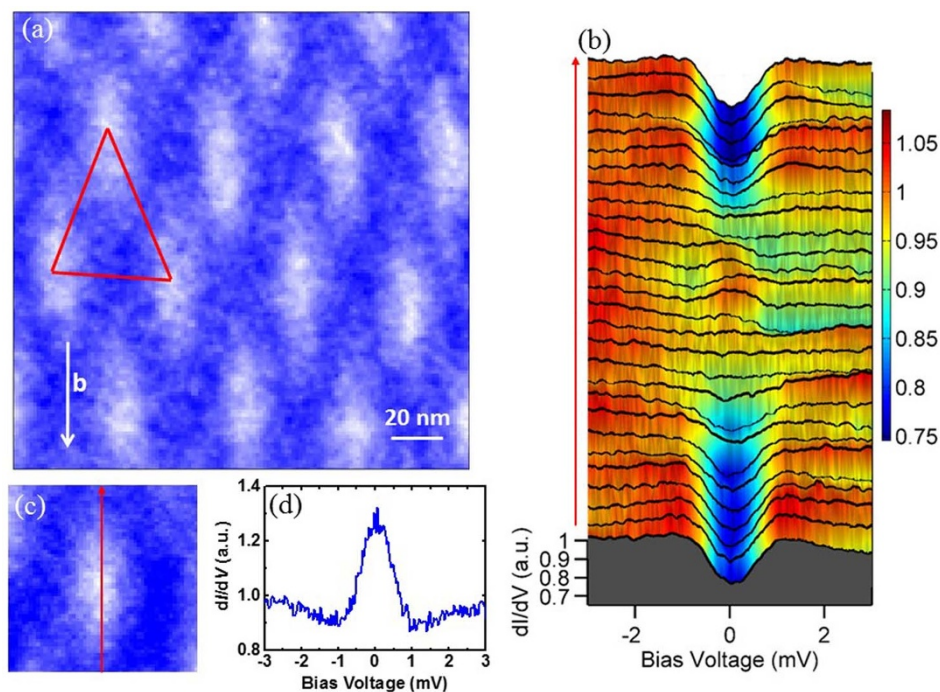


Figure 3 | Observation of elongated vortices and the CdGM states at 0.8 T. (a), 2D mapping of differential conductance measured at 0.45 K and 0.8 T in $\text{Ta}_4\text{Pa}_3\text{Te}_{16}$. It is clear to see the vortex array composed of elongated vortices. The distorted Abrikosov hexagonal lattice elongates in b -axis, and a typical triangle connecting three neighbored vortices has three internal angles of 45° , 74° , and 61° . (b), The spatially resolved tunnelling spectra measured across a vortex core. (c), The vortex selected for the measurement of spatial dependence of tunnelling spectra. The red arrow indicates the trace on which the tunnelling spectra shown in (b) were measured. (d), A tunnelling spectrum measured at the center of a vortex normalized with the one measured far away from the vortex centre.

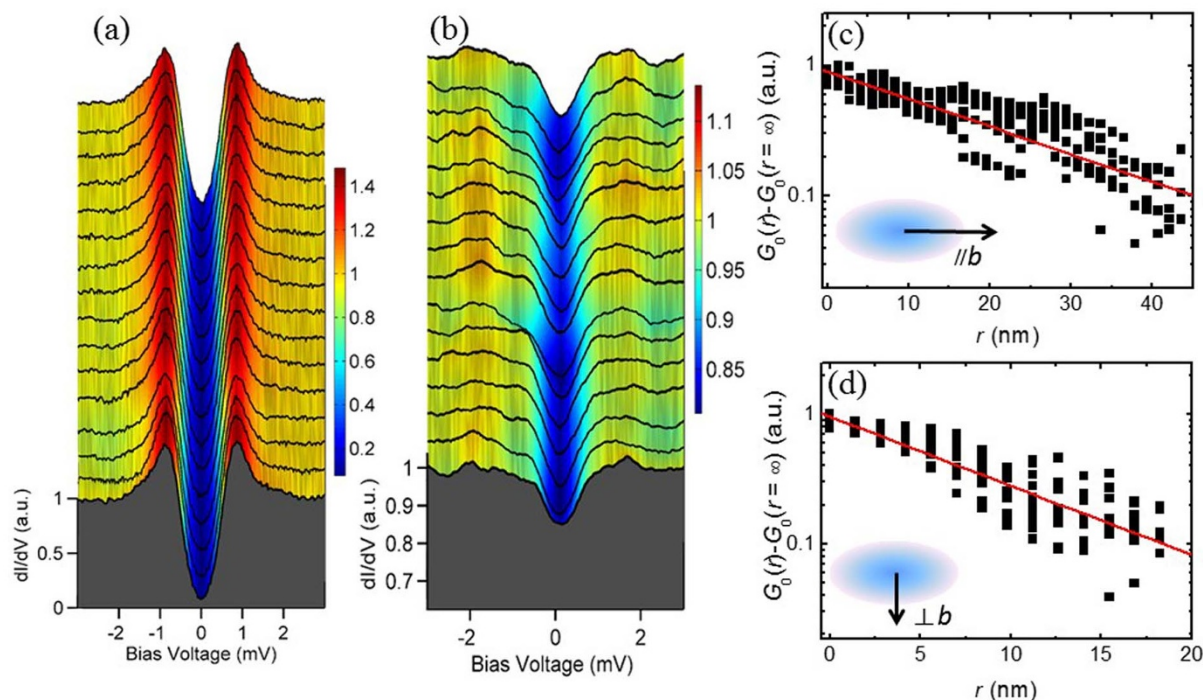


Figure 4 | Significant lifting of the zero-bias conductance at a magnetic field and determination of the in-plane anisotropy of coherence length. (a,b), The tunnelling spectra measured along the same line at zero magnetic field and 0.8 T far outside the vortex core at 0.45 K, respectively. (c,d), Spatial dependence of the differential conductance in semi-log plots across several different vortices along the long axis and short axis. The experimental data are fitted by the exponential decay formula (red lines), which leads to an average coherence length of $\xi_{//b} = 20.6$ nm and $\xi_{\perp b} = 8.2$ nm at the two perpendicular directions.

the radial dependences of the vortex-induced ZBC measured along b -axis and perpendicular to the b -axis (inset in Fig. 4(c) and (d)) are normalized to unity at the vortex centre and plotted in Figs. 4(c) and (d). Then an exponential decay law^{9,27} is fitted to the data. We find an average coherence length $\xi_{//b} = 20.6$ nm, $\xi_{\perp b} = 8.2$ nm, and the anisotropy $\xi_{//b}/\xi_{\perp b} \approx 2.5$.

For many type-II superconductors, the in-plane electronic property may have some anisotropy, but it is quite rare to see an elongated vortex. The significant elongation of the vortex in the present sample is remarkable. According to the DFT calculation¹⁷, the system contains several Fermi pockets or sheets with a clear one dimensional feature from β and γ sheets. Unfortunately, it has no report so far about how large the in-plane anisotropy of the Fermi velocity is. Furthermore there is no any study up to now about the magnitude of the gap value and anisotropy. Our results here will help to resolve these issues. Finally, the results may also initiate the interesting trend for studying the vortex physics. For an elongated vortex and distorted Abrikosov lattice, the vortex pinning force and the Bardeen-Stephen dissipation²⁸ coefficient need to be reconsidered, the vortex moving manner along b -axis and perpendicular to b -axis will certainly be different. Our discovery about the elongated vortex and the gap anisotropy will stimulate the study on the new superconductor $\text{Ta}_4\text{Pa}_3\text{Te}_{16}$ and may open a new area for the study of vortex motion and phase diagram with elongated vortices.

Methods

Sample growth and characterization. Single crystals $\text{Ta}_4\text{Pd}_3\text{Te}_{16}$ were grown by a self-flux method, which starts from Ta (99.9%), Pd (99%), and Te (99.999%) mixed in the mole ratio Ta : Pd : Te = 2 : 3 : 15. The synthesis is similar to the one reported previously¹⁵. The mixed powders were thoroughly ground and then sealed in an evacuated quartz tube. It was heated up to 950 °C in 20 hours and held at this temperature for 1 day, followed by cooling to 650 °C in 60 hours and finally cooling down to room temperature by shutting off the power of the furnace. DC magnetization measurements were carried out with a SQUID-VSM-7T (Quantum Design). The electrical resistivity was measured by the standard four-probe method

with current applied along the b -axis with a physical property measurement system (PPMS, Quantum Design).

STM measurements. The STM/S measurements were performed with an ultra-high vacuum, low-temperature, and high-magnetic-field scanning probe microscope USM-1300 (Unisoku Co., Ltd.). The samples were cleaved at room-temperature in ultra-high vacuum with a base pressure about 1×10^{-10} torr. In all STM/STS measurements, tungsten tips were used. The tips were treated by in situ e-beam sputtering and calibrated on a single crystalline Au(100) surface. To lower down the noise of the differential conductance spectra, a lock-in technique with an ac modulation of 0.1 mV at 987.5 Hz was used. Each tunneling spectrum shown in this Report was averaged with ten curves measured at the same position, and the spectra shown in Figs. 3(b) and 4(b) were smoothed to reduce the noise.

- Hoffman, J. E. *et al.* A four unit cell periodic pattern of quasi-particle states Surrounding vortex cores in $\text{Bi}_2\text{Sr}_2\text{CaCu}_2\text{O}_{8+\delta}$. *Science* **295**, 466–469 (2002).
- Pan, S. H. *et al.* STM Studies of the electronic structure of vortex cores in $\text{Bi}_2\text{Sr}_2\text{CaCu}_2\text{O}_{8+\delta}$. *Phys. Rev. Lett.* **85**, 1536–1539 (2000).
- Maggio-Aprile, I., Renner, C., Erb, A., Walker, E. & Fischer, Ø. Direct vortex lattice imaging and tunneling spectroscopy of Flux lines on $\text{YBa}_2\text{Cu}_3\text{O}_{7-\delta}$. *Phys. Rev. Lett.* **75**, 2754–2757 (1995).
- Hoogenboom, B. W., Renner, C., Revaz, B., Maggio-Aprile, I. & Fischer, Ø. Low-energy structures in vortex core tunneling spectra in $\text{Bi}_2\text{Sr}_2\text{CaCu}_2\text{O}_8$. *Physica C* **332**, 440–444 (2000).
- Hess, H. F., Robinson, R. B., Dynes, R. C., Valles, J. M. Jr & Waszczak, J. V. Scanning-Tunneling-Microscope observation of the Abrikosov flux lattice and the density of states near and inside a fluxoid. *Phys. Rev. Lett.* **62**, 214–216 (1989).
- Hess, H. F., Robinson, R. B. & Waszczak, J. V. Vortex-core structure observed with a scanning tunneling microscope. *Phys. Rev. Lett.* **64**, 2711–2714 (1990).
- Shan, L. *et al.* Observation of ordered vortices with Andreev bound states in $\text{Ba}_{0.6}\text{K}_{0.4}\text{Fe}_2\text{As}_2$. *Nature Phys.* **7**, 325–331 (2011).
- Hanaguri, T. *et al.* Scanning tunneling microscopy/spectroscopy of vortices in LiFeAs . *Phys. Rev. B* **85**, 214505 (2012).
- Yin, Y. *et al.* Scanning tunneling spectroscopy and vortex imaging in the iron pnictide superconductor $\text{BaFe}_{1.8}\text{Co}_{0.2}\text{As}_2$. *Phys. Rev. Lett.* **102**, 097002 (2009).
- Clem, J. R. Two-dimensional vortices in a stack of thin superconducting films: A model for high-temperature superconducting multilayers. *Phys. Rev. B* **43**, 7837–7846 (1991).
- Ooi, S., Mochiku, T. & Hirata, K. Periodic oscillations of Josephson-vortex flow resistance in $\text{Bi}_2\text{Sr}_2\text{CaCu}_2\text{O}_{8+\gamma}$. *Phys. Rev. Lett.* **89**, 247001 (2002).



12. Owen, C. S. & Scalapino, D. J. Vortex structure and critical currents in Josephson junctions. *Phys. Rev.* **164**, 538–544 (1967).
13. Bulaevskii, L. N., Ledvij, M. & Kogan, V. G. Vortices in layered superconductors with Josephson coupling. *Phys. Rev. B* **46**, 366–380 (1992).
14. Song, C. L. *et al.* Direct observation of nodes and twofold symmetry in FeSe Superconductor. *Science*. **332**, 1410–1413 (2011).
15. Jiao, W. H. *et al.* Superconductivity in a Layered Ta₄Pd₃Te₁₆ with PdTe₂ Chains. *J. Am. Chem. Soc.* **136**, 1284–1287 (2014).
16. Mar, A. & Ibers, J. A. Synthesis, crystal structure and electrical conductivity of a new layered ternary telluride Ta₄Pd₃Te₁₆. *J. Chem. Soc., Dalton Trans.* 639–641 (1991). DOI:10.1039/DT9910000639.
17. Singh, D. J. Multiband superconductivity of Ta₄Pd₃Te₁₆ from Te *p* states. *Phys. Rev. B* **90**, 144501 (2014).
18. Pan, J. *et al.* Observation of unconventional superconductivity in new layered superconductor Ta₄Pd₃Te₁₆. Preprinted at <http://arxiv.org/abs/1404.0371> (2014).
19. Hayashi, N., Isoshima, T., Ichioka, M. & Machida, K. Low-lying quasiparticle excitations around a vortex in quantum limit. *Phys. Rev. Lett.* **80**, 2921–2924 (1998).
20. Caroli, C., de Gennes, P. G. & Matricon, J. Bound fermion states on a vortex line in a type II superconductor. *Phys. Lett.* **9**, 307–309 (1964).
21. Fischer, Ø., Kugler, M., Maggio-Aprile, I., Berthod, C. & Renner, C. Scanning tunneling Spectroscopy of high-temperature superconductors. *Rev. Mod. Phys.* **79**, 353–419 (2007).
22. Dubois, C. *et al.* Node-like excitations in superconducting PbMo₆S₈ probed by scanning tunneling spectroscopy. *Phys. Rev. B* **75**, 104501 (2007).
23. Dynes, R. C., Narayanamurti, V. & Garno, J. P. Direct measurement of quasiparticle-lifetime broadening in a strong-coupled superconductor. *Phys. Rev. Lett.* **41**, 1509–1512 (1978).
24. Campbell, L. J., Doria, M. M. & Kogan, V. G. Vortex lattice structures in uniaxial superconductors. *Phys. Rev. B* **38**, 2439–2443 (1988).
25. Volovik, G. E. Superconductivity with lines of gap nodes-density-of-states in the vortex. *JETP Lett.* **58**, 469–473 (1993).
26. Zeng, B. *et al.* Anisotropic structure of the order parameter in FeSe_{0.45}Te_{0.55} revealed by angle-resolved specific heat. *Nat. Commun.* **1**, 112 (2010).
27. Song, C. L. *et al.* Dopant clustering, electronic inhomogeneity, and vortex pinning in iron-based superconductors. *Phys. Rev. B* **87**, 214519 (2013).
28. Bardeen, J. & Stephen, M. J. Theory of the motion of vortices in superconductors. *Phys. Rev.* **104**, A1197–A1207 (1965).

Acknowledgments

This work was supported by the Ministry of Science and Technology of China (973 projects: 2011CBA00102, 2012CB821403), NSF of China and PAPD.

Author contributions

The samples were grown by Y.F.L. and X.Y.Z. The transport measurements were done by Y.F.L., H.Y. and H.-H.W. The low-temperature STM/STS spectra measurements were performed by Z.Y.D., D.F., Z.W., H.Y., H.-H.W. and H.-H.W. coordinated the whole work. H.-H.W., Z.Y.D. and H.Y. wrote the manuscript, which was supplemented by other co-authors. All authors have discussed the results and the interpretation.

Additional information

Supplementary information accompanies this paper at <http://www.nature.com/scientificreports>

Competing financial interests: The authors declare no competing financial interests.

How to cite this article: Du, Z. *et al.* Anisotropic Superconducting Gap and Elongated Vortices with Caroli-De Gennes-Matricon States in the New Superconductor Ta₄Pd₃Te₁₆. *Sci. Rep.* **5**, 9408; DOI:10.1038/srep09408 (2015).



This work is licensed under a Creative Commons Attribution 4.0 International License. The images or other third party material in this article are included in the article's Creative Commons license, unless indicated otherwise in the credit line; if the material is not included under the Creative Commons license, users will need to obtain permission from the license holder in order to reproduce the material. To view a copy of this license, visit <http://creativecommons.org/licenses/by/4.0/>